Sensitivity optimization of injection-molded photonic crystal slabs for biosensing applications

Yousef Nazirizadeh,[1,*] Florian von Oertzen,[1] Klaus Plewa,[2] Nicole Barié,[3] Peter-Jürgen Jakobs,[3] Markus Guttmann,[3] Harald Leiste,[4] and Martina Gerken[1]

[1] *Institute of Electrical and Information Engineering, Christian-Albrechts-Universität zu Kiel, D-24143 Kiel, Germany*
[2] *Institute for Applied Materials – Material Process Technology, Karlsruhe Institute of Technology (KIT), D-76344 Eggenstein-Leopoldshafen, Germany*
[3] *Institute of Microstructure Technology, Karlsruhe Institute of Technology (KIT), D-76344 Eggenstein-Leopoldshafen, Germany*
[4] *Institute for Applied Materials – Applied Materials Physics, Karlsruhe Institute of Technology (KIT), D-76344 Eggenstein-Leopoldshafen, Germany*
*yn@tf.uni-kiel.de

Abstract: For label-free assays employing photonic crystal slabs (PCSs), the sensitivity is one of the most important properties influencing the detection limit. We investigate the bulk sensitivity and the surface sensitivity of 24 different PCSs fabricated by injection molding of PMMA and subsequent sputtering of a Ta_2O_5 high-index layer. The duty cycle of the linear grating is varied in steps of 0.1 between 0.2 and 0.7. Four different Ta_2O_5 layer thicknesses (89 nm, 99 nm, 189 nm, 301 nm) are deposited. Both bulk and surface sensitivity are optimal for a Ta_2O_5 layer thickness of 99 nm. The maximum bulk sensitivity of 138 nm/RIU is achieved for a duty cycle of 0.7, while the maximum surface sensitivity of 47 nm/RIU is obtained for a duty cycle of 0.5. Good agreement between experimental results and finite-difference time-domain (FDTD) simulations is observed. The PCSs sensitivity is linked to the mode intensity distribution.

©2013 Optical Society of America

OCIS codes: (160.5298) Photonic crystals; (160.1435) Biomaterials; (280.1415) Biological sensing and sensors.

References and links

1. J. S. Daniels and N. Pourmand, "Label-free impedance biosensors: opportunities and challenges," Electroanalysis **19**(12), 1239–1257 (2007).
2. G. Wu, H. Ji, K. Hansen, T. Thundat, R. Datar, R. Cote, M. F. Hagan, A. K. Chakraborty, and A. Majumdar, "Origin of nanomechanical cantilever motion generated from biomolecular interactions," Proc. Natl. Acad. Sci. U.S.A. **98**(4), 1560–1564 (2001).
3. D. Threm, Y. Nazirizadeh, and M. Gerken, "Photonic crystal biosensors towards on-chip integration," J. Biophotonics **16**, 1–16 (2012).
4. G. Gauglitz, "Direct optical sensors: principles and selected applications," Anal. Bioanal. Chem. **381**(1), 141–155 (2005).
5. S. S. Wang, R. Magnusson, J. S. Bagby, and M. G. Moharam, "Guided-mode resonances in planar dielectric-layer diffraction gratings," J. Opt. Soc. Am. A **7**(8), 1470–1474 (1990).
6. S. Fan and J. Joannopoulos, "Analysis of guided resonances in photonic crystal slabs," Phys. Rev. B **65**(23), 235112 (2002).
7. B. T. Cunningham, P. Li, B. Lin, and J. Pepper, "Colorimetric resonant reflection as a direct biochemical assay technique," Sens. Actuators B Chem. **81**(2-3), 316–328 (2002).
8. B. T. Cunningham, P. Li, S. Schulz, B. Lin, C. Baird, J. Gerstenmaier, C. Genick, F. Wang, E. Fine, and L. Laing, "Label-free assays on the BIND system," J. Biomol. Screen. **9**(6), 481–490 (2004).
9. Y. Nazirizadeh, U. Bog, S. Sekula, T. Mappes, U. Lemmer, and M. Gerken, "Low-cost label-free biosensors using photonic crystals embedded between crossed polarizers," Opt. Express **18**(18), 19120–19128 (2010).
10. I. M. White and X. Fan, "On the performance quantification of resonant refractive index sensors," Opt. Express **16**(2), 1020–1028 (2008).
11. M. El Beheiry, V. Liu, S. Fan, and O. Levi, "Sensitivity enhancement in photonic crystal slab biosensors," Opt. Express **18**(22), 22702–22714 (2010).
12. U. Geyer, J. Hauss, B. Riedel, S. Gleiss, U. Lemmer, and M. Gerken, "Large-scale patterning of indium tin oxide electrodes for guided mode extraction from organic light-emitting diodes," J. Appl. Phys. **104**(9), 093111 (2008).
13. L. J. Guo, "Nanoimprint lithography: methods and material requirements," Adv. Mater. **19**(4), 495–513 (2007).

14. C.-H. Chang and W.-B. Young, "Fabrication of the plastic component for photonic crystal using micro injection molding," Microsyst. Technol. **16**(6), 941–946 (2010).
15. E. Cho, B. Kim, S. Choi, J. Han, J. Jin, J. Han, J. Lim, Y. Heo, S. Kim, G. Y. Sung, and S. Kang, "Design and fabrication of label-free biochip using a guided mode resonance filter with nano grating structures by injection molding process," J. Nanosci. Nanotechnol. **11**(1), 417–421 (2011).
16. C. Vannahme, S. Klinkhammer, A. Kolew, P.-J. Jakobs, M. Guttmann, S. Dehm, U. Lemmer, and T. Mappes, "Integration of organic semiconductor lasers and single-mode passive waveguide into a PMMA substrate," Microelectron. Eng. **87**(5-8), 693–695 (2010).
17. Y. Nazirizadeh, J. G. Müller, U. Geyer, D. Schelle, E.-B. Kley, A. Tünnermann, U. Lemmer, and M. Gerken, "Optical characterization of photonic crystal slabs using orthogonally oriented polarization filters," Opt. Express **16**(10), 7153–7160 (2008).
18. M. Huang, A. A. Yanik, T. Y. Chang, and H. Altug, "Sub-wavelength nanofluidics in photonic crystal sensors," Opt. Express **17**(26), 24224–24233 (2009).
19. N. A. Mortensen, S. Xiao, and J. Pedersen, "Liquid-infiltrated photonic crystals: enhanced light-matter interactions for lab-on-a-chip applications," Microfluid. Nanofluid. **4**(1-2), 117–127 (2008).
20. A. Szeghalmi, E. B. Kley, and M. Knez, "Theoretical and experimental analysis of the sensitivity of guided mode resonance sensors," J. Phys. Chem. C **114**(49), 21150–21157 (2010).

1. Introduction

Label-free assays became in the past decade a powerful tool for many applications in bio-analytics and are expected to gain more in importance, e.g., for pharmaceutical industry or academic research. The physics behind label-free measurements ranges from electrical or mechanical to optical methods [1–4]. However, only few of these methods have reached commercial realization. There are three important criteria for successful commercialization: high sensitivity, high-throughput capability, and cost efficiency. All these criteria are fulfilled for biosensing based on photonic crystal slabs (PCSs).

The PCS, which is a periodic nanostructure in a high index slab, serves as the transducer. It provides optical modes penetrating the analyte area and interacting with refractive index changes on the surface. In transmission or reflection experiments these modes are the origin of guided mode resonances (GMRs) [5,6]. GMRs shift in their central wavelength with changed refractive index. Surface functionalization leads to specific binding of an analyte to the surface. The position of resonance's central wavelength depends on the resulting refractive index change and is used as a measure of the binding. The central wavelength is determined either via a spectrometer [7,8] or using a spectrally limited light source, which is matched to a resonance in order to transform the spectral shift into an inexpensive photometric experiment [9]. The detection limit of such measurements is a function of the optical detection method, the line width of the resonance, and the PCS's sensitivity defined as the resonance wavelength shift $\Delta\lambda$ divided by the refractive index change Δn [10]. The bulk sensitivity is determined by a refractive index change in the bulk region above the PCS. As it is easy to measure and compare, many optimization efforts focus on enhancement of the bulk sensitivity. Most label-free assays, however, employ binding and thus a refractive index change at the surface and hence a surface sensitivity is a more appropriate figure of merit for sensitivity optimization.

The challenge for the success of PCS label-free assays is not only to achieve high sensitivities, but also to fabricate the PCS consumables cost-efficiently. In general the PCS can be realized either in a symmetric or an asymmetric geometry. In the symmetric geometry the high index slab is surrounded by the analyte material, which means that the substrate material is absent or far away. This leads to a high sensitivity for these structures [11]. In the asymmetric geometry, on the other hand, the high index slab is in direct contact with the substrate. The asymmetric geometry brings two advantages: inexpensive fabrication and mechanical stability. Today, the most economical way to fabricate asymmetric PCSs is the replication of a master and subsequent high-index layer deposition. For a high number of consumables the inexpensive fabrication of the master is not as crucial as the inexpensive replication step. Hence, the master can be fabricated using electron-beam lithography or laser interference lithography [12] with a subsequent etching procedure. For the replication of this master nanoimprint lithography (NIL) can be used [13]. This fabrication method, however, incorporates several steps, such as the application of the photoresist layer to the substrate surface, the imprint step itself, and the exposure with ultraviolet radiation. An alternative way

for replication is injection molding of the master (also known as mold insert) [14,15], which is basically only one step. Injection molding has been established as an efficient way to fabricate plastic items ranging from low-level products, e.g., yogurt cups, up to high-tech parts, e.g., Blu-ray discs.

In this paper we describe the fabrication of PCSs using injection molding and subsequent sputtering of a high-index layer in section 2. 24 different PCS were fabricated with different duty cycles of the periodic nanostructure and variation of the high index layer thickness. In section 3 the bulk sensitivities of the different PCSs are evaluated and in section 4 the surface sensitivities are analyzed. Experimental results are compared to finite-difference time-domain (FDTD) simulations. The simulation results are used to explain the changes in sensitivity. Conclusions are given in section 5.

2. Photonic crystal slab (PCS) fabrication

For PCS fabrication we chose injection molding for nanostructured nickel mold replication and sputtering for the high-index layer. At first a master was fabricated using electron-beam lithography. The nanostructure of this master was written in a 100-nm thick resist on a 4-inch silicon wafer. The periodicity of the nanostructure was chosen to be 400 nm and the duty cycle of the linear grating was varied from 0.2 to 0.7. After development thin films of chromium and gold were deposited on the master structure to prepare a conductive layer for the electroforming process. The subsequent electroplating from a nickel sulphamate electrolyte yielded a 0.5-mm thick round nickel shim with a diameter of about 86 mm [16]. The high thickness was required, as the injection molding process uses high injection pressures up to 1150 bar. Finally, the shim was cut into nine equal-sized mold inserts with final dimensions of 16 mm x 17 mm using wire-cut EDM.

To fabricate PCSs the nanostructured nickel mold insert was assembled to a specific adapter. In the next step this adapter was mounted into the two-part injection-molding tool. As schematically shown in Fig. 1(a) 245°C hot PMMA was injected into a down to 0.4 mbar evacuated and 135°C warm injection molding tool, which was opened after cooling down to 45°C. As molding material PMMA Degalan G7E type from Evonik Industries AG was used. An additional baking step for thermal relaxation is employed after the injection-molding step to reduce the residual mechanical stress in the material, which may cause unwanted polarization rotation. In Fig. 1(b) scanning electron microscope (SEM) images of the nanostructures on the nickel mold and its replica are shown for a PCS duty cycle of 0.3. In the last fabrication step the nanostructured replicas were sputtered with Ta_2O_5. This resulted in PCSs with the following high index layer thicknesses: 89 nm, 99 nm, 189 nm, and 301 nm. In Fig. 1(c) photographs of the nickel mold and a PCS are shown.
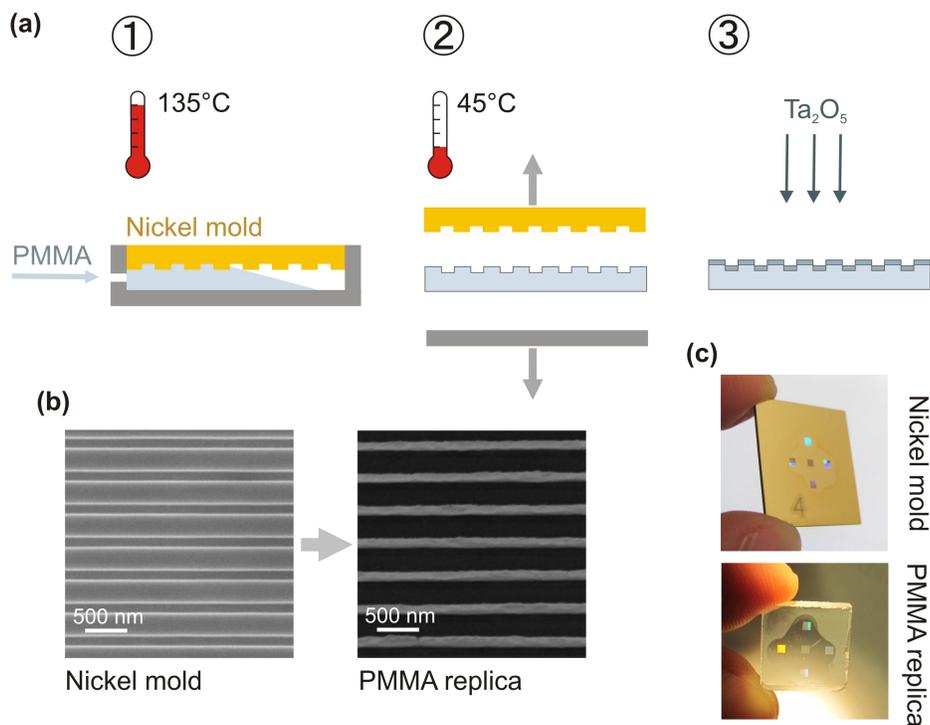
Fig. 1. (a) Schematic of PCS fabrication using injection molding and sputtering. Hot PMMA is injected in the injection molding tool, composed of a nickel mold and sidewalls. After cooling down the tool is opened and the nanostructured substrate is obtained. In a sputtering process a Ta_2O_5 layer is deposited on the substrate. (b) SEM images and (c) photographs of the nickel mold and the PMMA replica.

3. Bulk sensitivity

To perform sensitivity measurements we use the setup shown in Fig. 2(a). In this transmission experiment the light source is a halogen lamp providing white light. To filter background light, which is not interacting with the PCS, we use crossed polarization filters before and after the PCS [17]. GMRs are collected with a microscope objective (20x) and are directed to a spectrometer. The surface of the PCS is accessible and is covered with different liquids. The liquid surface is terminated with a cover glass. In order to determine the bulk sensitivity, two liquids with different refractive indices are used one after the other. The refractive index change Δn on the surface of the PCS results in a shift of the GMRs. The shift $\Delta\lambda$ of the GMR with the highest intensity is used to calculate the bulk sensitivity $\Delta\lambda/\Delta n$ as shown exemplary in Fig. 2(b).
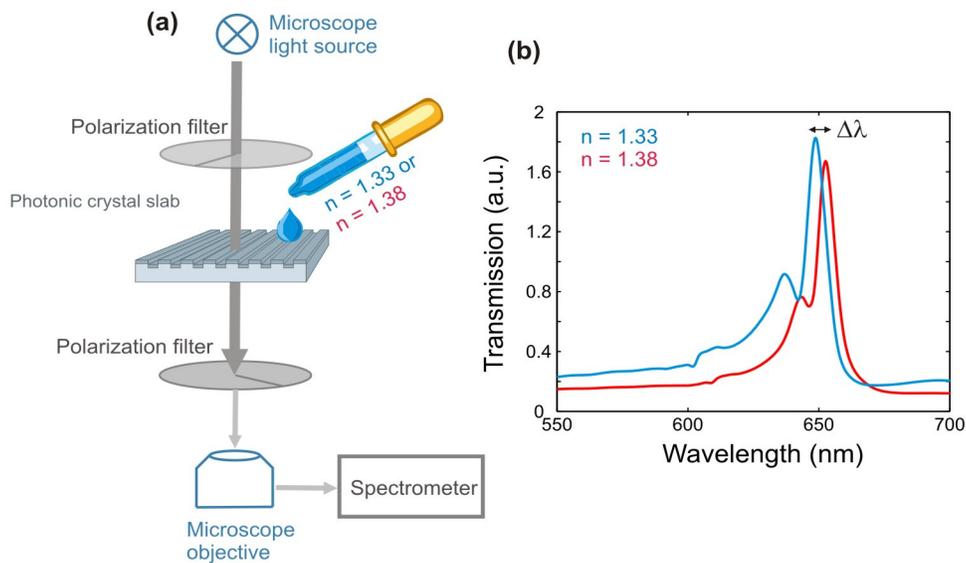
Fig. 2. (a) Setup for sensitivity measurement: A halogen lamp serves as the light source. The transmitted light is collected by a microscope objective and directed to a spectrometer. Crossed polarization filters are used to suppress the background light. (b) Transmission spectrum for the PCS with a duty cycle of 0.4 and a Ta_2O_5 layer thickness of 99 nm for two different liquids on the surface. The GMR's spectral shift $\Delta\lambda$ is defined as the shift of the highest maximum. The bulk sensitivity is calculated as $\Delta\lambda/\Delta n$ = 4.6 nm/(1.38-1.33) RIU = 92 nm/RIU.

To mimic an environment relevant to real label-free assays we used liquids with refractive indices of 1.33 (100% water) and 1.38 (ca. 71% water and ca. 29% glycerol) as shown in Fig. 3(a). Transmission measurements were performed for all fabricated PCSs with both liquids and bulk sensitivities were calculated. In Fig. 3(b) these results are shown. The bulk sensitivities range from 31.5 nm/RIU for a duty cycle of 0.2 and a high-index layer thickness of 301 nm to 138 nm/RIU for a duty cycle of 0.7 and a high-index layer thickness of 99 nm, which is a 4.38 fold enhancement. Here, two general tendencies are observable. First, the bulk sensitivity increases with the duty cycle. Second, a maximum for the bulk sensitivity is observed for a high-index layer thickness of 99 nm. In publications [11,18], which discuss PCSs without substrate, the authors observe increased bulk sensitivity, while decreasing the slab thickness. On the other hand, however, they observed increased bulk sensitivity for increased hole diameter, which is contrary to our observations.

To understand this opposite tendency we performed two-dimensional finite-difference time-domain (FDTD) simulations using a commercial software (FDTD Solution from Lumerical Inc.). Periodic boundary conditions were used to terminate the simulation cell in the direction of the periodicity and perfectly matched layers (PML) at the top and bottom of the simulation cell. The unit cell of the PCS, which was placed in the center of the simulation cell, was covered either with a refractive index of 1.33 or 1.38. A plane wave source positioned in the upper part of the simulation cell illuminated the PCS. A monitor placed in the lower part of the simulation cell collected the transmission. In the transmission spectra the resonance maximum was determined and used to calculate the bulk sensitivity. In Fig. 3(c) bulk sensitivities for the TE mode are shown, as this polarization was dominant in experimental transmission measurements. The simulation results confirm results from the experiments.
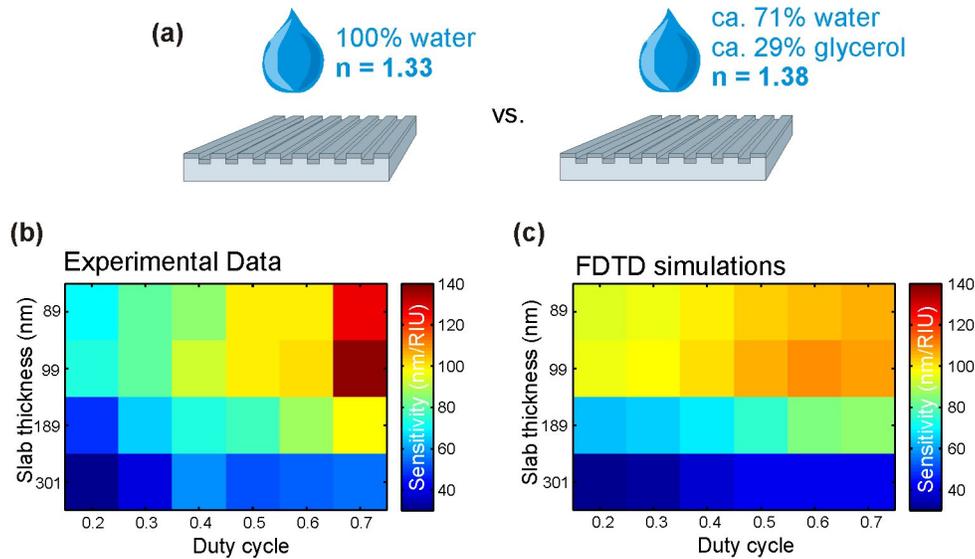
Fig. 3. Bulk sensitivity results. (a) To calculate the bulk sensitivity, two transmission experiments with two different refractive indices on the surface of the PCS were performed. (b) Experimental bulk sensitivity as a function of high index slab thickness and periodicity duty cycle. (c) Simulated bulk sensitivity as a function of high index slab thickness and periodicity duty cycle.

The resonance shift induced by refractive index change is a function of the ambient refractive index. In Fig. 4(a) transmission simulations through a PCS with a duty cycle of 0.5 and a slab thickness of 99 nm show exemplarily the resonance shift in the range of 1.33 to 1.38. This shift, however, is not linear and leads to a non-constant bulk sensitivity as shown in Fig. 4(b). Hence, our experimental and simulated results as shown in Fig. 3 are an average of the bulk sensitivities in this range.
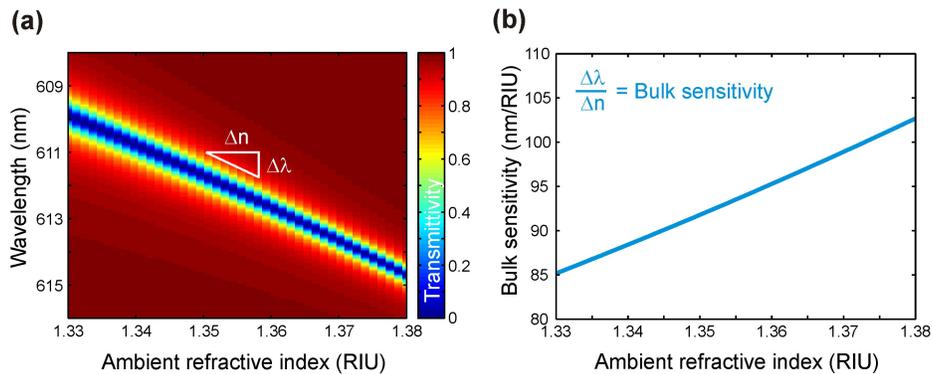

Fig. 4. (a) Transmission spectra through a PCS with a duty cycle of 0.5 and a slab thickness of 99 nm as a function of the ambient refractive index. (b) Bulk sensitivity calculated from the resonance shift.

In Fig. 5 the simulated mode intensity distributions are plotted for three different high-index layer thicknesses. We can define three areas in these plots: substrate area, high index area, and

analyte area. Bulk sensitivity increases for a higher fraction of the mode in the analyte area [11,19]. For the two smaller thicknesses (89 nm and 99 nm) we observe that the largest part of the mode is located in the substrate and analyte area. The substrate area contains a higher fraction of the mode, as it has a higher refractive index compared to the analyte. For the largest layer thickness (189 nm), however, the fraction of the mode in the high index area is much increased corresponding to a smaller fraction of the mode in the analyte. This explains the reduced bulk sensitivity for an increased high-index layer thickness.

In Fig. 6 the mode intensity for three different duty cycles and a high index layer thickness of 99 nm is plotted. In these plots we observe that the mode is pulled up for a higher duty cycle resulting in an increased interaction area with the analyte and a higher bulk sensitivity.
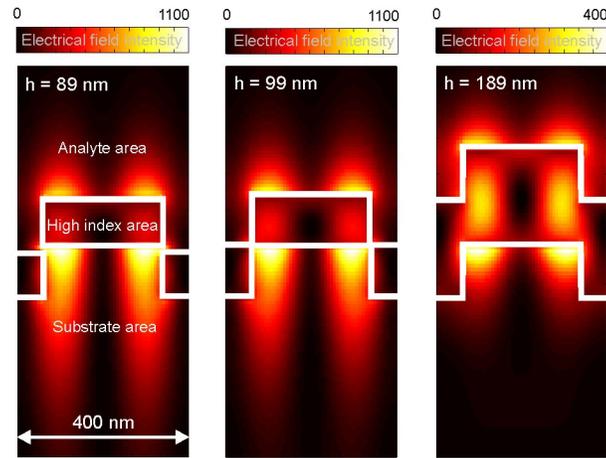

Fig. 5. Simulated mode intensity distribution for three different high-index layer thicknesses. For the highest high-index layer thickness, the largest mode fraction is observed in the high-index area. Hence, the fraction of the mode in the analyte area is decreased and the bulk sensitivity drops.
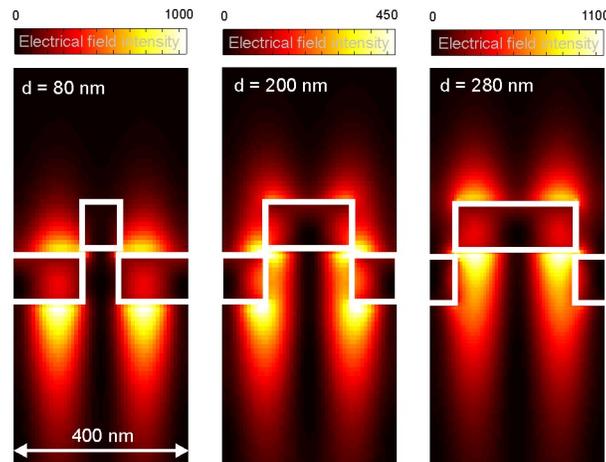

Fig. 6. Simulated mode intensity distribution for three different duty cycles (0.2, 0.5, 0.7) of the periodicity. Higher duty cycle pushes the mode up and allows for a larger interaction area with the analyte. This improves the bulk sensitivity.

4. Surface sensitivity

Although the bulk sensitivity is easy to measure and good to compare with other label-free methods, it is only an approximation for the sensitivity of the transducer in real biochemical assays. Surface sensitivity, which is the resonance shift induced by a refractive index change only on the surface area of the PCS divided by the refractive index change, is a more accurate measure for the transducer's sensitivity. Therefore, in an optimization procedure the surface sensitivity should be on focus.

The variety of biochemical assays does not allow for a single definition of the surface sensitivity. The thickness and the refractive index of the biolayer depend on the type of assay. One way to define the surface sensitivity is to determine the resonance shift $\Delta\lambda$ induced by the biolayer thickness change Δl [20]. In this paper we propose to use the resonance shift resulting from the refractive index change of the biolayer with a constant thickness. To obtain the surface sensitivity we divide the resonance shift $\Delta\lambda$ by the refractive index change Δn. This definition allows for a better comparison with the bulk sensitivity. In Fig. 7 we simulated the sensitivity for different biolayer thicknesses with a refractive index of 1.38 surrounded by water (n = 1.33). The sensitivity approaches the bulk sensitivity for large biolayer thicknesses. As 25 nm is a relevant thickness for biochemical assays, we choose this thickness for further surface sensitivity calculations in this work.
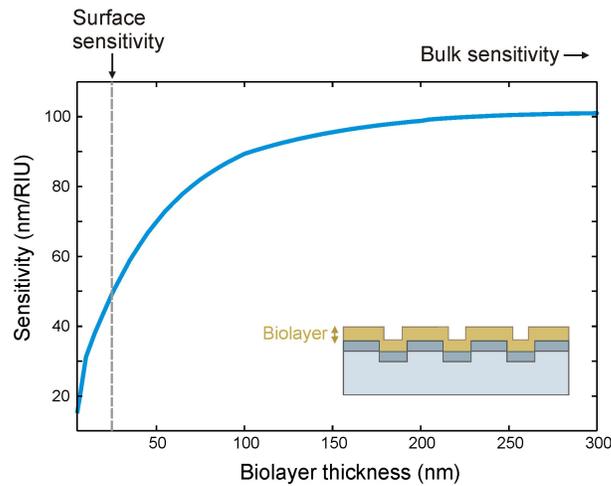

Fig. 7. Sensitivity as a function of the biolayer thickness. The sensitivity is obtained by dividing the resonance shift (structure with biolayer compared to structure without biolayer) by the refractive index difference of the biolayer (n = 1.38) and the ambient medium (n = 1.33). In this paper we define the surface sensitivity as the sensitivity obtained for a 25-nm biolayer. For higher biolayer thicknesses the sensitivity approaches the bulk sensitivity.

To realize a local refractive index change on the surface of the PCS we used thermal evaporation and deposited a 25-nm lithium fluoride (LiF) layer on top of the PCS. With a refractive index of 1.39 it provides similar optical properties as a biological film. The same PCSs used for the bulk sensitivity measurements, were now employed in these experiments. We compared the resonance wavelength with and without the LiF layer always surrounded by water as shown in Fig. 8(a). The surface sensitivity was calculated by dividing the resonance shift by the refractive index difference of water and LiF. The experimental results are presented in Fig. 8(b). The surface sensitivities range from 3.25 nm/RIU for a duty cycle of 0.3 and a high-index layer thickness of 301 nm to 47.15 nm/RIU for a duty cycle of 0.5 and a high-index layer thickness of 99 nm, which is a 14.5 fold enhancement.
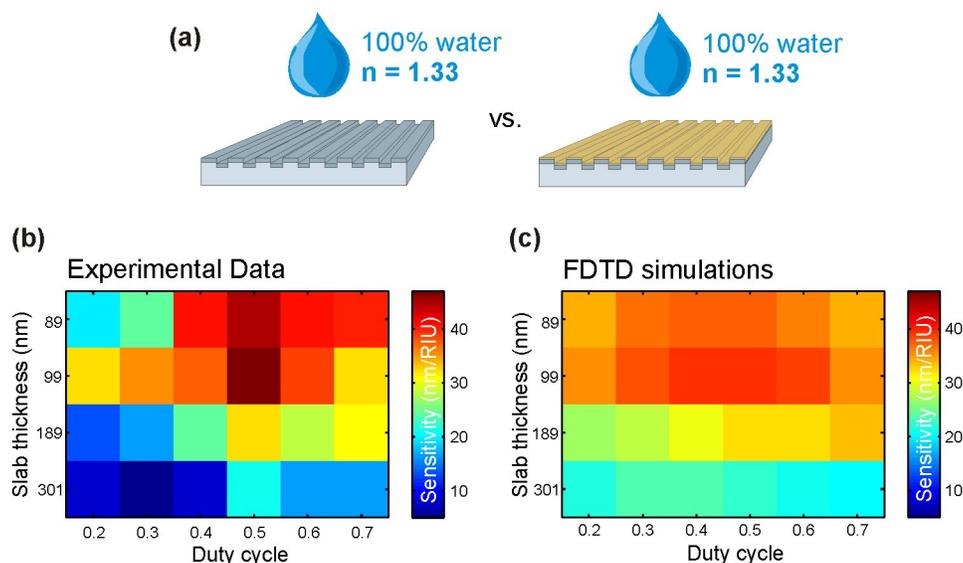
Fig. 8. Surface sensitivity results. (a) To calculate the surface sensitivity, two transmission experiments with and without a 25 nm LiF layer on the surface of the PCS were performed. In both experiments the PCS was covered with water. (b) Experimental surface sensitivity as a function of high-index slab thickness and periodicity duty cycle. (c) Simulated surface sensitivity as a function of high-index slab thickness and periodicity duty cycle.

The surface sensitivity results in Fig. 8 show a different behavior than the ones for the bulk sensitivity in Fig. 3. A sensitivity maximum is still observed for a high-index layer thickness of 99 nm, but in contrary to the bulk measurements a maximum in sensitivity is obtained for a duty cycle of 0.5. FDTD simulations, which were carried out analogous to bulk sensitivity simulations described in section 3, confirm this observation (Fig. 8(c)). The origin of this behavior may be explained by studying Fig. 8. As the mode is pulling up to the analyte area, it passes a state, where it has a maximum interaction area with the surface of the nanostructure. For a more detailed analysis of the experimental results the exact deposition profile of the LiF layer as well as the Ta_2O_5 layer needs to be considered.

5. Conclusion

We fabricated PCSs using injection molding and subsequent high-index layer deposition. In order to investigate the influence of the high-index layer thickness and the duty cycle of the periodicity on the sensitivity, 24 different PCSs geometries were evaluated in experiment and simulation. Experimentally, a maximum bulk sensitivity of 138 nm/RIU is achieved for a Ta_2O_5 layer thickness of 99 nm and a duty cycle of 0.7, while the maximum surface sensitivity of 47.15 nm/RIU results for a Ta_2O_5 layer thickness of 99 nm and a duty cycle of 0.5. These best designs show sensitivity improvements of 4.38 fold for bulk sensitivity and 14.5 fold for surface sensitivity compared to poor designs. With this experimental series, general tendencies are established for optimal bulk and surface sensitivity values in asymmetric PCSs. Large high-index layer thicknesses pull the mode into the high-index layer and reduce the sensitivity. In contrast to symmetric PCSs, the bulk surface sensitivity was higher for larger duty cycles, as the mode is pulled towards the analyte area. The surface sensitivity, on the other hand, is maximal for an intermediate duty cycle. Thus, bulk sensitivity and surface sensitivity are found to be different for the same PCS and should be optimized separately depending on the application. The optimized injection-molded PCSs presented here are promising as transducers for label-free assays. They offer a high sensitivity, are cost-efficient in fabrication and mechanically stable.